Axial mass fraction measurements in a 300kA dense plasma focus

L. S. Caballero Bendixsen,[1,a)] S. C. Bott-Suzuki,[1,b)] S. W. Cordaro,[1] M. Krishnan,[2] S. Chapman,[2] P. Coleman,[3] and J. Chittenden[4]

[1]*Center for Energy Research, University of California, San Diego, La Jolla, California 92093, USA*
[2]*Alameda Applied Sciences Corporation, San Leandro, California 94577, USA*
[3]*Evergreen Hill Sciences, Philomath, Oregon 97370, USA*
[4]*Imperial College London, South Kensington, London SW7 2AZ, United Kingdom*

The dynamics and characteristics of the plasma sheath during the axial phase in a $\sim$300 kA, $\sim$2 kJ dense plasma focus using a static gas load of Ne at 1–4 Torr are reported. The sheath, which is driven axially at a constant velocity $\sim$10^5 m/s by the j $\times$ B force, is observed using optical imaging, to form an acute angle between the electrodes. This angle becomes more acute (more parallel to the axis) along the rundown. The average sheath thickness nearer the anode is 0.69 ± 0.02 mm and nearer the cathode is 0.95 ± 0.02 mm. The sheath total mass increases from $1 \pm 0.02 \mu$g to $6 \pm 0.02 \mu$g over the pressure range of 1–4 Torr. However, the mass fraction (defined as the sheath mass/total mass of cold gas between the electrodes) decreases from 7% to 5%. In addition, the steeper the plasma sheath, the more mass is lost from the sheath, which is consistent with radial and axial motion. Experimental results are compared to the Lee code when 100% of the current drives the axial and radial phase. *Published by AIP Publishing.*
[http://dx.doi.org/10.1063/1.4962679]

I. INTRODUCTION

The Dense Plasma Focus (DPF), independently developed by Mather[1] and Fillipov *et al.*,[2] has been studied since the 1960s. Models of the macroscopic physics of each phase of the DPF and scaling laws were available in the late 1970s.[3,4] Since its invention, most of the scientific effort has pivoted around its fusion promise and its remarkable radiation source capabilities (i.e., X-rays, neutrons).[5,6] To a lesser extent, the community has examined the dynamics of the plasma sheath moving in the axial and radial phases. For example, Bdot sensors in the axial and radial phases have been used to record the sheath velocity and current distribution,[7] Schlieren images have studied the dynamics of the radial phase,[8] and X-ray pinhole imaging has characterized typical hot spot size during the pinch phase.[9] In general, the work has focused on the independent analysis of each phase and little work has been reported in connecting all the phases of the discharge. There are still many open questions on how the previous phase affects the next and how initial conditions may influence the pinch.

The work presented here examines the experimental results on the dynamics and general characteristics of the axial phase of the DPF. The sheath velocity, driving angle, thickness, total mass, and mass fraction are reported. The aim here is to set boundary conditions (or limitations) for these key parameters and estimate the mass fraction pushed by the Lorentz force for the first time. It is hoped that this experimental work will help with the refinement of 3D numerical simulations.

The majority of the numerical simulations of DPFs have used 1-D models such as the code developed by Lee.[10] However, the DPF current sheath is inherently 2-D during the coaxial rundown and subsequent radial implosion phases, and there are radial and axial mass flows in both phases. The 1-D models assume purely the axial flow followed by purely the radial flow; they must therefore assign adjustment factors to the accelerated mass and the driving current, to consider these 2-D effects. The four adjustment factors (two each for axial and radial current and mass) are varied to give a reasonable fit of the Lee code current to the measured current.

This work presents the measurements of the (average) axial mass fraction that is accelerated, based on the optical emission measurements of the sheath. Earlier work by one of the authors[11] had shown that all of the current flowed in the radial phase, implying by induction that all of the current must also have been convected axially. The work here shows that measured average axial mass fraction and the measured current (not a fraction) can be compared with the 1-D Lee code, provided that the origin of the computed current is delayed with respect to the measured current. Thus, a single fitting parameter (the sheath motion onset delay) is shown to suffice to match the computed and measured currents, rather than the two free parameters.

II. THE EXPERIMENT

A. Dense plasma focus

The experiments were performed on the DPF-3 plasma focus—a Mather-type DPF at Alameda Applied Sciences Corporation (AASC) that operates at a typical shot rate of 0.1 Hz, but that is designed (with cooling) to operate at up to 10 Hz.[12] The DPF is run at Vc = 11 kV with a stored energy of E$_{stored}$ $\sim$ 1.7 kJ using Ne gas at 1–4 Torr. The DPF coaxial

a)lscb@ucsd.edu; http://www.p3ucsd.com
b)sbottsuzuki@ucsd.edu

geometry has an anode 30 mm in diameter and 113 mm long, with a cathode that consists of 16 rods, 3 mm in diameter, and 105 mm in length, on a 60 mm diameter circle. The alumina insulator is 25 mm long and 43 mm in outer diameter. The short circuit inductance (to the vacuum interface) was measured to be $L_0 = 19 nH$, for a capacitance $C_0 = 28.8 \ \mu F$ and a loop resistance $R_0 = 7 \ m\Omega$. Even without cooling, the high repetition rate of DPF-3 allows a typical run of 150–300 of shots per gas load at a repetition rate of 6 shots/min. A day's run gives 1000 s of shots whose data are analysed to provide statistically significant interpretations of the salient physics. The DPF was run with two different peak currents in order to explore if a modest difference, of about 12%, would produce significant variations in the behaviour of the sheath. The two different conditions are labeled Current A and Current B in all the figures shown below (Current A is the higher current).

B. Diagnostics

A set of diagnostics to capture the electrical and physical parameters of the plasma during the axial, radial, and pinch phases of the DPF was implemented. This set includes a Rogowski coil and high voltage probe for current and voltage vs. time; a non-intrusive optical imaging array to observe the axial phase;[13] laser interferometry, shadowgraphy, and Faraday rotation; an array of magnetic pick up coils to measure the enclosed current in the radial phase and a diamond radiation detector (DRD) measures the X-radiation output of the pinch. The data from all the diagnostics are recorded on each shot by several 1 GHz, 5 GS/s, 8-bit, Tektronix TVS645A digitizers, and digital SLR cameras. The data are then read into a laptop computer via a LabView script. Figure 1 illustrates how a typical run of 200+ shots is analysed by a MatLab routine. In this example, the average Rogowski coil (built into the base of the cathode plate) waveform shows dI/

dt vs. time. A clear indication of the pinch is shown by the deep dip in the dI/dt waveform when the inductance is increased abruptly (~100 ns) by the pinch. The average current waveform is also displayed, where the dashed vertical lines represent the start and end of the different phases of the DPF (i.e., breakdown (BP), axial (AP) and radial (RP) phases). The current is computed by a MatLab code for each Rogowski coil waveform using the cumulative trapezoidal numerical integration method. Previously, the Rogowski coil was calibrated by matching the known current response of an RLC circuit and its numerically integrated Rogowski coil response. In addition to these waveforms, pinch time and peak current per shot, the average (red solid line) and the standard deviation (red dash lines) for these parameters are also presented. In both cases, the 2-sigma dispersion of these values is low, ~2% for both pinch time and peak current. Throughout the first ~50 shots of each run, the pinch time decreases at a constant rate before stabilizing around the average. This effect is due to the warming up of the electrode[14] and happens in every run, though this is a similar effect to the conditioning of the DPF.

The work presented here is restricted to the axial phase of the discharge. The axial dynamics were measured using a non-perturbing axial diagnostic developed by Veloso.[13] This optical diagnostic was implemented to measure the last third of the axial phase of the discharge, which is highlighted in red in the dI/dt and current waveforms of Figures 1(a) and 1(b). The diagnostic consists of a converging lens arrangement (f = 280 mm, magnification M ~ 3, depth of field ~3 mm) that collects light from the moving plasma sheath and projects this visible emission onto a 2-by-5 fiber-optic array. The lines-of-sight in the anode-cathode gap are shown in Figure 2. The fiberoptic lines are attached to an array of alternately positively and negatively biased fast photodiodes (SFH250V). Two independent digitizer channels are used to record the photodiode signals, one per light-collecting column. The
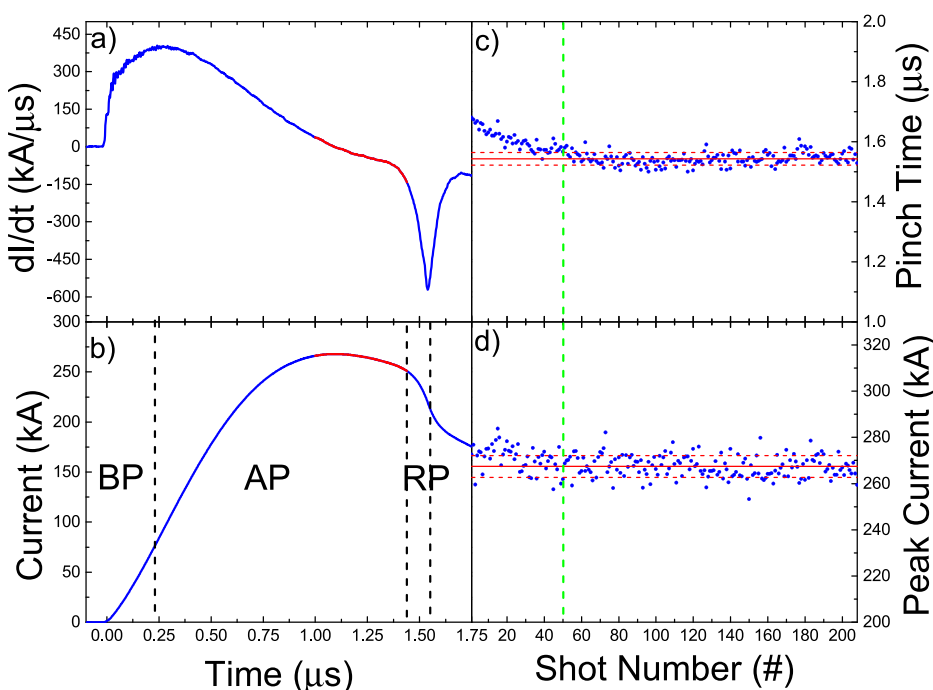

FIG. 1. Average waveforms dI/dt (a) and current (b) are presented showing the breakdown (BP), axial (AP) and radial phases (RP). Pinch time (c) and peak current (d) per shot with their corresponding averages and standard deviation are exhibited.
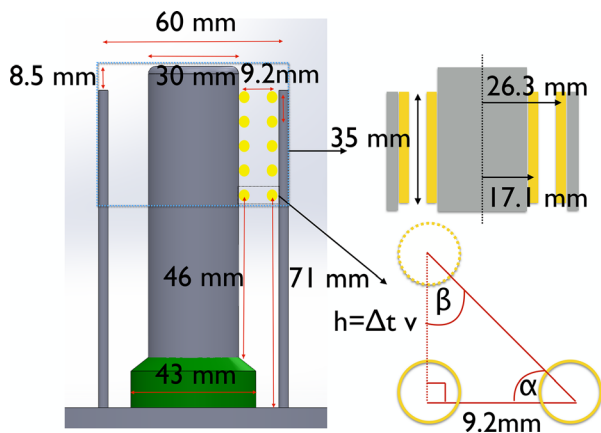
FIG. 2. DPF electrodes illustration showing the light-collecting positions for matrix diagnostic, light-collecting volume and triangulation approximation.

image positions are fixed for all the runs and the columns observe the plasma sheath closest to the anode and closest to the cathode, respectively.

Figure 3 explains the analysis of the collected light signals. Figure 3(a) shows the characteristic waveforms for each light-collecting column (i.e., from the anode and cathode). It displays two oscillating waveforms of crests and troughs, corresponding to the self-emission from the plasma when the sheath passes each collimating position. The characteristic crests and troughs are due to positive and negative biasing circuit configuration of each photodiode array, which allows a better separation of the rise-times of the traces. This simple configuration allows a detailed characterisation of the plasma sheath in the axial phase. Analyzing this information allows deduction of the sheath velocity, driving angle, thickness, mass and mass fraction.

By plotting each individual, fixed light-collecting position versus the time measured from each crest and trough, Figure 3(b), is obtained. A constant slope is observed,

implying a constant velocity of the sheath at both ends of the sheath (i.e., v_a anode and v_c cathode). Furthermore, when observing in greater detail both the waveforms displayed in Figure 3(a), it is noted that the first two crests on each waveform (anode and cathode) have a time delay Δt, which indicates that the sheath closer to the anode reaches the lowest light-collecting position (at h = 71 mm) first. This feature is repeated throughout all the subsequent collecting positions. This is a clear indication that the sheath is tilted at an angle relative to the anode. Approximating the profile of the sheath as the straight hypotenuse of a triangle, with the base of the triangle being the distance between both collecting-light columns and the height being the displacement of the sheath during the time delay, $\Delta h = \Delta t \, v_a$, the driving angle is given by $\beta = \arctan(9.2/\Delta h)$, as illustrated in Figure 2. The measured angles in the last third of the axial phase are displayed in Figure 3(c). The sheath thickness, d, shown in Figure 3(d) is calculated in two steps. From the photodiode signal, the thickness is given by $d = v \cdot \Delta\tau$, where v is the average velocity of the sheath (i.e., v_a anode and v_c cathode) and $\Delta\tau$ is the full width at high maximum (FWHM) for each crest and trough, showing the behaviour along the axial phase. In order to avoid any misinterpretation of which of the light emitting volumes correspond to the plasma sheath, the thickness is cross-calibrated with interferometric images at the edge of the cathode.

To determine the total mass of the sheath throughout the axial phase, the snowplow model[15] approach is used. The plasma sheath is lifted and accelerated by the Lorentz force, $j \times B$, where j is the current density flowing through the sheath and B is the induced magnetic field. In this model, the force is equal to the change in the momentum, p, over time (i.e., dp/dt). A constant velocity, v, of the sheath in the region of interest was measured, as shown in Figure 3(b). Therefore, the force equation that governs the movement of the plasma sheath is given by
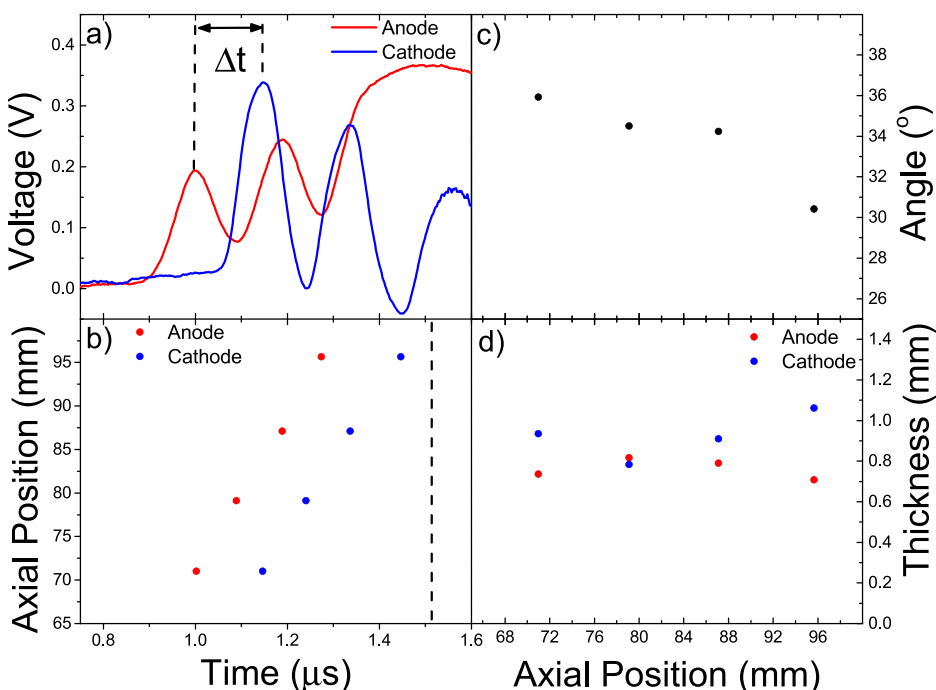

FIG. 3. Photodiode analysis example which shows (a) the characteristic photodiode waveform response, (b) time at which the sheath passes through each collecting-light position, (c) the plasma sheath driving angle and (d) thickness at different positions along the rundown.

$$j \times B = v \frac{d\rho}{dt}, \tag{1}$$

where ρ is the mass density of the plasma sheath, for both the anode and cathode ends. By integrating Equation (1), the total mass added to the sheath in the course of the measurement is given by

$$m = \frac{2 \cdot l \times 10^{-7}}{v \cdot r} \int_{t_1}^{t_2} I^2(t)dt, \tag{2}$$

where l is the plasma sheath thickness and r is the radius at which the sheath velocity is measured (i.e., at the anode and cathode), and t_1 and t_2 are the times at which the diode starts and ends its measurement. For simplicity, the average sheath thickness is used here to do the calculation. The calculated mass corresponds to the total mass the magnetic force is able to push at the constant velocity observed experimentally.

The above analysis is carried out for each individual shot by a MatLab script. This enables an accurate understanding of the physics of each run, with a statistical analysis (based on 100s or 1000s of shots rather the usual 10s of shots) of each parameter of interest and a comparison as a function of gas pressure. The peak current and pinch time are presented in Figure 4, where each of the points in the graph represents the analysis of hundreds of shots. The same is true for the subsequent figures. This clearly shows a linear dependence of both parameters, which increases with pressure. A later pinch indicates that the sheath moves more slowly at higher pressure. This is corroborated by the data in Figure 5(a) which shows that the sheath velocity decreases linearly with pressure. These data also indicate that the anode end of the sheath moves faster for all pressures, with the exception of 1 Torr. For this pressure, the characteristic photodiode waveform, for the anode end, was not well defined, making it difficult to interpret suggesting a poorly formed plasma sheath. A faster anode sheath suggests that the driving angle should become steeper as the sheath moves along the axis. This is evident in Figure 5(c), which shows the driving angle measured at two different axial positions,
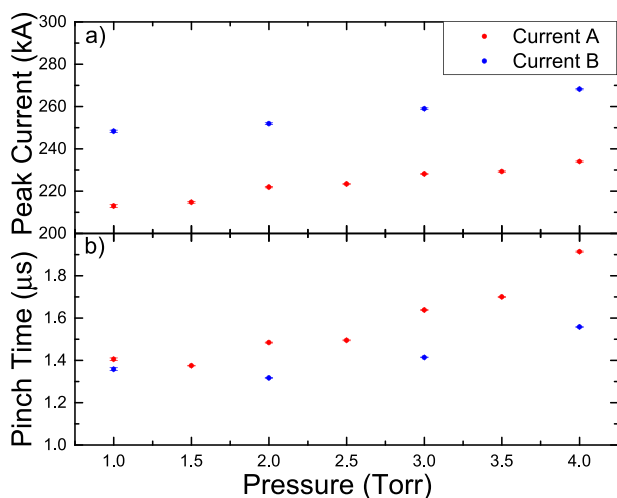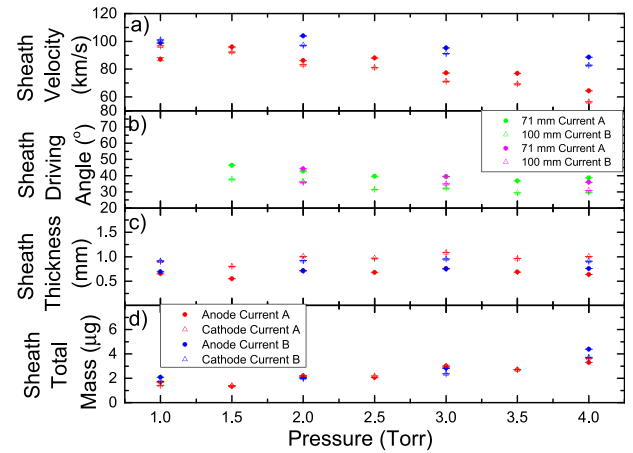

FIG. 5. Average values for the sheath velocity, driving angle, thickness, and total mass dragged as a function of load pressure for the anode and cathode end. Each point considers hundreds of shots.

71 mm and 100 mm, from the base of the electrodes. This corroborates the above notion that a difference in velocity at the ends of the sheath results in a steeper angle. On average, the angle decreases by $7.8° \pm 0.4°$. Since the magnetic field falls as $1/r$ away from the anode, one expects a higher force and hence higher velocity nearer the anode for the same mass fraction, thereby forming an acute angle between the plasma sheath and the anode.

The plasma sheath becomes thinner closer to the anode and thicker closer to the cathode when moving along the axis (see Figure 3(d)). However, the average sheath thickness shown in Figure 5(c) remains constant as a function of load pressure. On average, the anode end is 0.69 ± 0.02 mm thick and the cathode end is 0.95 ± 0.02 mm thick. The plasma sheath ploughs into neutral gas, which is ionized in the sheath, thereby adding more mass to the sheath. Figure 5(d) shows the total mass at both ends of the sheath, showing that more mass is added when the pressure is higher, as expected. In addition, for each individual pressure the mass seems to be equal at both ends of the sheath. However, there is a difference in the total mass available to be ionized at the different pressures in the two regions of interest (anode and cathode). These two volumes are approximated as concentric hollow cylinders with a thickness of 3 mm (light-collecting diameter) centered at 17.1 mm and 26.3 mm radii, respectively, with a total length of 35 mm. This approximate geometry corresponds to the visible light collection volume at the anode and cathode, as illustrated in Figure 2. By comparing the calculated sheath mass and the total available mass of cold gas in the volume of interest, the mass fraction can be calculated. Figure 6 shows this mass fraction as a function of gas load pressure and how it varies with the driving angle at the end of the rundown. This shows that at a steeper angle, more mass is lost from the sheath.

Figure 4 shows the different peak currents explored. The pinch time is reduced, on average, by 17% for the higher current that drives the sheath at a faster velocity. This is corroborated in Figure 5(a) which shows that the velocity is 22% faster for the higher current runs. From the above, it is clear that all the trends already discussed are true for both

FIG. 4. Peak current (a) and pinch time (b) as a function of load pressure.
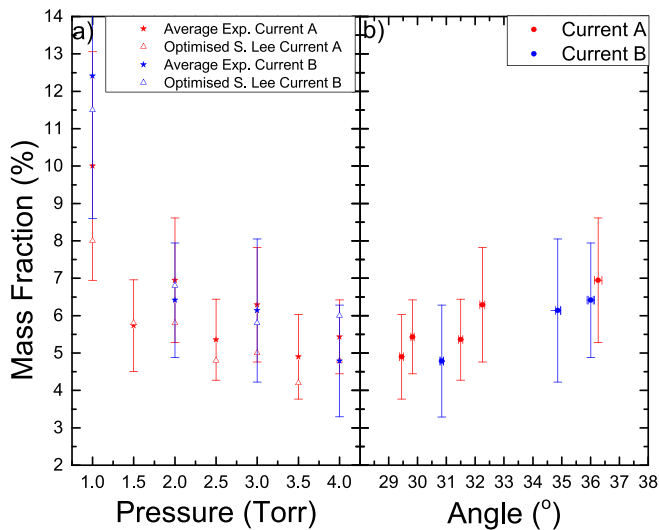
FIG. 6. Mass fraction as a function of gas pressure and sheath driving angle.

explored current patterns. On the other hand, it is observed that the driving angle, sheath thickness and mass are not significantly affected by this 12% difference in driving current.

III. DISCUSSION

A general characterization of the plasma sheath during the last 1/3 of the axial phase of a dense plasma focus has been presented. Assuming no acceleration of the sheath throughout the rundown, the linear fit shown in Figure 3(b) describes the dynamics of the sheath. Using this constant velocity ansatz, the different phases can be delineated, as shown by the dashed vertical lines in Figure 1. In addition, the time since the plasma is formed—after the breakdown phase—the lift-off, when the plasma sheath moves in the insulator-cathode gap, can be estimated.[16]

The Lee 1-D Code[10,17] has become the standard in the field, enabling amongst other things the design of new DPFs and comparison of the performance of existing DPFs with experimental results. The code uses the snowplow model with a finite slab of plasma, perpendicular to the anode, which is pushed by the Lorentz force. The model begins the description with the plasma sheath at the edge of the insulator moving towards the open end of the electrodes. The model uses 11 parameters determined by the experiment (i.e., gas load, geometrical and electrical characteristics). In addition, there are 4 free parameters, mass and current fractions in the axial and radial phases (i.e., massf, massfr, currf and currfr, respectively), which are varied in order to get a close fit to the experimental current waveform. The code is usually run assuming a current fraction currf = currfr ~ 0.7, which means that 70% of the total available current drives the sheath. However, experimental results have demonstrated that all the current is coupled in the radial phase of a plasma focus,[11] requiring that all the current must also be driving the axial phase. Furthermore, considering a temperature $T \sim 3\,eV$, sheath density $n \sim 10^{18}\,cm^{-3}$, plus the measured velocity $v \sim 10^5\,m/s$ and sheath thickness $d \sim 1\,mm$ yields a Magnetic Reynolds number $R_m \sim 6$. This plasma sheath should be fully MHD in the axial phase, with

the magnetic streamlines frozen into the fluid streamlines. A fraction of the current cannot detach from this highly magnetised sheath as that would require resistive diffusion or a much lower magnetic Reynolds number.

Following these two arguments, simulations using the Lee 1-D model were carried out assuming that the plasma sheath is driven by 100% of the current (i.e., currf = currfr = 1). The example in Figure 7(a) clearly shows a good agreement when massf = 0.045 and massfr = 0.15 are used. The optimised axial mass fraction fits within the experimental error bars estimated from the optical imaging measurements (see Figure 6). However, this excellent fit does require a delay of the onset of the Lee current by 180 ns with respect to the measured current. The 1-D Lee code makes no provision to capture this transient phase that exists in all DPFs. The higher voltage machines might have a much shorter transient phase, but it exists nevertheless. Furthermore, all DPFs that use an axial insulator must create a sheath that the first lift-off radially (inverse pinch phase) and only then does it begin its axial motion. The delay assigned to the computed trace in Figure 7(a) is a simple adjustment factor to account for all these effects. A single parameter (shown here to link to real physical processes) suffices to match with the measured current. Figure 7(b) uses the same experimental waveform as in Figure 7(a), this time though the free parameters are: currf = 0.7, currfr = 0.8, massf = 0.023, massfr = 0.1 and a current onset delay of 160 ns. The fit is as good as the one in Figure 7(a) that used fewer free parameters. This example shows the arbitrariness of the multi-parameter fit that is traditionally used in the Lee model. This example illustrates that when the mass fractions are measured (as done for the axial phase in this work), the full current may be used but provided that the Lee current is shifted in time to account for latency in sheath breakdown and the inverse pinch phase before axial acceleration.

The work presented here has focused on the axial phase of the discharge. The optimised S. Lee mass fraction as a function of gas pressure is added to Figure 6. This clearly
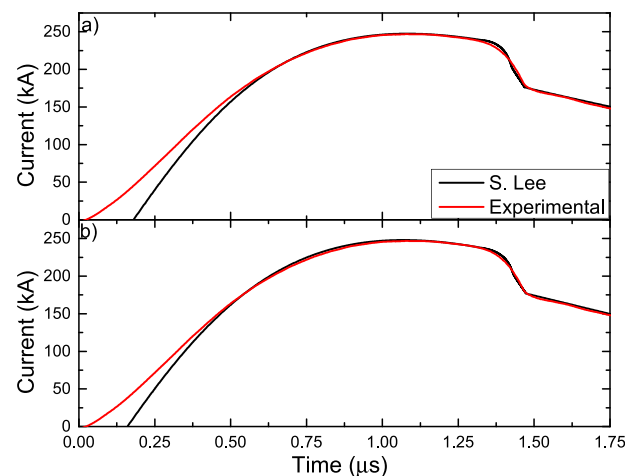

FIG. 7. Experimental and Lee code waveforms comparison for a single shot. The Lee code was run with the following parameters: (a) currf = currfr = 1, massf = 0.045 and massfr = 0.15, and delay time of 180 ns and (b) currf = 0.7, currfr = 0.8 massf = 0.023 and massfr = 0.1, and delay time of 160 ns.

shows that the optimised values fit within the experimental error bars. Moreover, it seems that the mass fraction follows a trend with pressure. This trend suggests that the higher the background pressure, the less effective is the ionization process, and less mass is needed to achieve a pinch. In addition, the axial mass fraction and the driving angle at the end of the rundown were compared, see Figure 6. This comparison shows that when the sheath is driven at a steeper angle, more mass is lost from the sheath (i.e., radial flux out of the sheath leads to a lower mass fraction).

IV. FINAL REMARKS

The plasma sheath has been characterized in the last third of the axial phase in the DPF-3 device using Ne gas load at 1–4 Torr. The plasma in the axial phase moves at a constant velocity on the order of 10^5 m/s. This plasma sheath moves 7% faster at the anode end, forming an acute angle between the electrodes, which gets steeper along the axial phase. On average, the thickness of the anode and cathode ends is 0.69 ± 0.02 mm and 0.95 ± 0.02 mm, respectively. However, when looking at sheath behaviour at different positions in the axial phase, the sheath at the anode end gets thinner while at the cathode end it gets thicker. The total mass in the last third of the axial phase is of 1 ± 0.02 μg to 6 ± 0.02 μg in the pressure range 1–4 Torr. The dragged mass fraction varies from 7% to 5% scaling approximately linearly as the sheath steepness and inversely with fill pressure. It is expected that the results presented here give better initial considerations and constrains in 3D numerical simulations.

ACKNOWLEDGMENTS

[1]J. W. Mather, "Investigation of the high-energy acceleration mode in the coaxial gun," Phys. Fluids **7**(11), S28 (1964).

[2]N. V. Fillipov, T. I. Fillipova, and V. P. Vinogradov, "Dense high- temperature plasma in a non-cylindrical Z-pinch compression," Nucl. Fusion Suppl. **2**, 557–587 (1962).

[3]M. Krishnan, "The dense plasma focus: A versatile dense pinch for diverse applications," IEEE Trans. Plasma Sci. **40**(12), 3189–3221 (2012).

[4]D. E. Potter, "Numerical studies of the plasma focus," Phys. Fluids **14**(9), 1911 (1971).

[5]A. Bernard, H. Bruzzone, P. Choi, H. Chuaqui, V. Gribkov', J. Herrera, K. Hirano, A. Krejci, S. Lee, C. Luo, F. Mezzetti, M. Sadowski, H. Schmidt, K. Ware, C. S. Wong, and V. Zoita, "Scientific status of plasma focus research," J. Moscow. Phys. Soc. **8**, 93–170 (1998).

[6]W. Stygar, G. Gerdin, F. Venneri, and J. Mandrekas, "Particle beams generated by a 612.5 kJ dense plasma focus," Nucl. Fusion **22**(9), 1161–1172 (1982).

[7]M. A. Mohammadi, S. Sobhanian, M. Ghomeishi, E. Ghareshabani, M. Moslehi-Fard, S. Lee, and R. S. Rawat, "Current sheath dynamics and its evolution studies in Sahand Filippov type plasma focus," J. Fusion Energy **28**(4), 371–376 (2009).

[8]L. Soto, C. Pavez, J. Moreno, M. J. Inestrosa-Izurieta, F. Veloso, G. Gutiérrez, J. Vergara, A. Clausse, H. Bruzzone, F. Castillo, and L. F. Delgado-Aparicio, "Characterization of the axial plasma shock in a table top plasma focus after the pinch and its possible application to testing materials for fusion reactors," Phys. Plasmas **21**(12), 122703 (2014).

[9]P. G. Burkhalter, G. Mehlman, D. A. Newman, M. Krishnan, and R. R. Prasad, "Quantitative x-ray emission from a DPF device," Rev. Sci. Instrum. **63**(10), 5052–5055 (1992).

[10]S. Lee, "Plasma focus radiative model: Review of the lee model code," J. Fusion Energy **33**(4), 319–335 (2014).

[11]N. Qi, S. F. Fulghum, R. R. Prasad, and M. Krishnan, "Space and time resolved electron density and current measurements in a dense plasma focus Z-pinch," IEEE Trans. Plasma Sci. **26**(4), 1127–1137 (1998).

[12]B. L. Bures, M. Krishnan, and R. E. Madden, "Relationship between neutron yield and macroscale pinch dynamics of a 1.4-kJ plasma focus over hundreds of pulses," IEEE Trans. Plasma Sci. **39**(12), 3351–3357 (2011).

[13]F. Veloso, J. Moreno, A. Tarifeño-Saldivia, C. Pavez, M. Zambra, and L. Soto, "Non-intrusive plasma diagnostics for measuring sheath kinematics in plasma focus discharges," Meas. Sci. Technol. **23**(8), 087002 (2012).

[14]B. L. Bures, M. Krishnan, and C. James, "A plasma focus electronic neutron generator," IEEE Trans. Plasma Sci. **40**(4), 1082–1088 (2012).

[15]N. A. Krall and A. W. Trivelpiece, *Principles of Plasma Physics* (McGraw-Hill, New York, 1973).

[16]F. Veloso, A. Tarifeño-Saldivia, C. Pavez, J. Moreno, M. Zambra, and L. Soto, "Plasma sheath kinematics and some implications on the modeling of very low energy plasma focus devices," Plasma Phys. Controlled Fusion **54**(9), 095007 (2012).

[17]S. Lee, S. H. Saw, P. C. K. Lee, R. S. Rawat, and H. Schmidt, "Computing plasma focus pinch current from total current measurement," Appl. Phys. Lett. **92**(11), 111501 (2008).